Scalable Triple Cation Mixed Halide Perovskite - $BiVO_4$ Tandems for Bias-Free Water Splitting

Virgil Andrei,[a] Robert L. Z. Hoye,[b] Micaela Crespo-Quesada,[a] Mark Bajada,[a] Shahab Ahmad,[c] Michael De Volder,[c] Richard Friend,[b] and Erwin Reisner*[a]

Strong interest exists in the development of organic-inorganic lead halide perovskite photovoltaics and of photoelectrochemical (PEC) tandem absorber systems for solar fuel production. However, their scalability and durability have long been limiting factors. In this work, we reveal how both fields can be seamlessly merged together, to obtain scalable, bias-free solar water splitting tandem devices. For this purpose, state-of-the-art cesium formamidinium methylammonium (CsFAMA) triple cation mixed halide perovskite photovoltaic cells with a nickel oxide (NiO_x) hole transport layer are employed to produce Field's metal-epoxy encapsulated photocathodes. Their stability (up to 7 h), photocurrent density (–12.1±0.3 mA cm^{-2} at 0 V vs. RHE) and reproducibility enables a matching combination with robust $BiVO_4$ photoanodes, resulting in 0.25 cm^2 PEC tandems with an excellent stability of up to 20 h and a bias-free solar-to-hydrogen efficiency of 0.35±0.14%. The high reliability of the fabrication procedures allows scaling of the devices up to 10 cm^2, with a slight decrease in bias-free photocurrent density from 0.39±0.15 mA cm^{-2} to 0.23±0.10 mA cm^{-2} due to an increasing series resistance. To characterise these devices, a versatile 3D-printed PEC cell was also developed. The modular PEC cell represents an affordable alternative to existing designs and can be easily adjusted for a broad range of samples. Overall, these findings shed further light on the factors required to bring both perovskite photovoltaics and photoelectrocatalysis into large-scale applications, revealing some key aspects for device fabrication, operation and implementation.

Keywords: perovskite photocathodes, $BiVO_4$ photoanodes, PEC tandems, scalability, water splitting.

1 Introduction

As society's energy demands increase, the production and storage of sustainable energy becomes a critical issue.[1–4] While photovoltaic (PV) modules may cover this demand on their own, large scale applications still require alternatives to batteries and supercapacitors for a more effective energy storage and transport.[1,2,5–9] From this perspective, solar fuels (e.g. H_2, CO) represent a promising option, due to their high specific energy density, which makes them favourable for transport or conversion to more conventional liquid fuels. To harness sunlight into chemical energy, several routes have been developed spanning from connecting photovoltaic modules to separate electrolysers,[10] to developing solution immersed photoelectrochemical (PEC) systems.[11–13] Since the energy conversion efficiency of a single photoabsorber is theoretically limited[14] (below 12.7% for water splitting to produce H_2[15]), tandem systems of two complementary absorbers are preferably employed for PV, PEC and hybrid PV-PEC applications.[12,15–18] Such photoelectrode tandem systems are particularly interesting for the field of solar fuels, where one of the main aims is driving electrochemical processes (e.g. water splitting, or CO_2 reduction) without applying an additional electrochemical bias.[19] The end goal for those PEC systems is the broad implementation of lightweight monolithic (i.e. wireless) devices, which are also known as artificial leaves.[20]

Although several examples of using tandem photoabsorbers for water splitting have been previously reported, most of them were hybrid systems combining a photoanode with a wired/buried silicon,[21–24] or dye-sensitised[25–35] PV cell. In this case, the use of double- or multi-junction photovoltaics was ocasionally required to obtain an appropiate driving force for water splitting.[21,22,36–40] In contrast, only a few photoelectrocatalytic tandems employing oxide,[41–46] or silicon[47–50] based photocathodes could operate under bias-free conditions. For example, 0.6 V were required to reach a 0.11% applied bias solar-to-hydrogen (AB-STH) efficiency in $Cu_2O|NiO_x$-WO_3 tandems,[42] whereas a more optimized FTO|Au|Cu_2O|Al:ZnO|TiO_2|RuO_x-$BiVO_4$|Co-Pi system could later reach a bias-free photocurrent density of 0.32 mA cm^{-2} and a stability of 1.4 h.[45] Similarly, the combination of a silicon-based photocathode with a $BiVO_4$|TiCo photoanode could achieve a maximal AB-STH efficiency of 0.59% at 0.6 V bias,[47] which was later improved to a bias-free value of 0.57% using a p-Si nanoarray|Pt-Mo:$BiVO_4$|Co-Pi tandem.[48]

Due to the rapid growth in the efficiency of lead halide perovskite photovoltaics, rising from the initial 3.8% reported by Miyasaka et al. in 2009[51] to beyond 22% nowadays,[52] these photoabsorbers have also attracted attention from the solar fuel community. The initial prototypes involved wired systems, where several solar cells were connected in series to separate electrocatalysts, resulting in successful proton,[53–57] CO_2,[58] or H_2S reduction.[59] Since the use of wired systems provides several disadvantages by requiring gas separating membranes, wiring, external connections and additional device packaging,[13,60] several recent reports proposed more compact designs for PEC-PV tandem devices.[61,62] Nevertheless, to prevent degradation of the perovskite layer, the photovoltaic component was again physically separated from the solution, with a conductive wire ensuring the connection to the electrocatalyst. Such devices mainly combined a perovskite cell with a high band gap oxide layer (i.e. $BiVO_4$,[61,63–66] WO_3,[67] TiO_2,[68] or hematite[62,69,70]) to drive water splitting,[63] or CO_2 reduction.[71] In those cases, bias-free devices could be achieved due to the high open circuit voltage (V_{OC}) of the perovskite component, which enabled a good overlap between the cathodic and anodic photocurrents.

While previous attempts to directly interface the regular structure perovskite surface to an electrolyte solution through a thin nickel layer have produced a moderate stability of 10-30 min with photocurrents varying between 2-17 mA cm^{-2} for the oxygen evolution reaction,[72–74] a significant improvement was recently demonstrated in our group by employing the low melting point Field's metal (FM) instead.[75] This InBiSn alloy could simultaneously provide encapsulation and electrical contact to

[a] *Christian Doppler Laboratory for Sustainable SynGas Chemistry, Department of Chemistry, University of Cambridge, Lensfield Road, Cambridge CB2 1EW, United Kingdom. E-mail: reisner@ch.cam.ac.uk; Web: http://www-reisner.ch.cam.ac.uk*

[b] *Optoelectronics Group, University of Cambridge, Cavendish Laboratory, J J Thomson Avenue, Cambridge CB3 0HE, United Kingdom.*

[c] *NanoManufacturing group, Department of Engineering, 17 Charles Babbage Road, Cambridge CB3 0FS, United Kingdom.*

a platinum nanoparticle (Pt-NP) catalyst, sustaining an encouraging hydrogen generation photocurrent of $-6.9\pm1.8\,mA\,cm^{-2}$ at 0 V against the reversible hydrogen electrode (RHE) beyond one hour.[75] In this case, an inverse structure perovskite cell was necessary to collect electrons for the proton reduction at the outer device surface (see schematic depictions in Fig. 1). With an onset potential of 0.95 ± 0.03 V vs. RHE, this initial system represented a promising example of a perovskite-based photocathode, on the basis of which wireless tandems for solar fuel production could be developed.

While most of these initial results employed the moisture, air and temperature sensitive methylammonium lead triiodide ($MAPbI_3$) perovskite,[51,76] more recent photovoltaic reports have shown that improvements in both efficiency and stability can be obtained when using complex precursor solutions. In particular, mixtures including the formamidinium (FA) and methylammonium cations (MA), together with iodide and bromide anions, achieved efficiencies beyond 20%,[77,78] whereas the addition of further alkali cations (e.g. cesium, magnesium, or potassium) have increased both efficiency (above 21%) and stability (beyond a few weeks).[79–85] Still, the limited scalability of perovskite cells remained an issue until very recently, when large scale deposition procedures such as spray coating, doctor blading or vacuum techniques[86] started to be optimized alongside spin coating[82,87] for larger photovoltaic modules, leading to efficiencies between 10-16% for areas above $36\,cm^2$.[16,82,88,89]

Accordingly, although organic-inorganic lead halide perovskite photovoltaics have experienced a rapid development in performance within the last decade, the field has mostly continued to suffer from the same challenges of device up-scaling as photoelectrocatalysis. To address some of those issues, in this work we investigate the scalability of tandem photoelectrochemical (PEC) devices for water splitting, combining a CsFAMA triple cation perovskite-driven photocathode with a bismuth vanadate photoanode. To gain a complete understanding of the limiting factors, the performance and scalability are investigated separately for the photovoltaic cells and for the derived photocathodes. In order to evaluate devices of various sizes, we also propose a straightforward design for a modular 3D-printed PEC cell, which can be easily assembled or adapted for large scale studies.

2 Experimental section

Preparation of perovskite solution

A 1.0 M solution of the $FAMA_{0.22}Pb_{1.1}I_{3.2}Br_{0.66}$ perovskite precursor was made by dissolving methylammonium bromide (MABr, 24.3 mg), lead bromide ($PbBr_2$, 80.0 mg), formamidinium iodide (FAI, 172.0 mg), and lead iodide (PbI_2, 507.1 mg) in a 1000 μL mixture consisting of N,N-dimethylformamide (DMF, 510 μL), dimethyl sulfoxide (DMSO, 340 μL), and 1-methyl-2-pyrrolidone (NMP, 150 μL). A 1.5 M stock solution of cesium salt was prepared by dissolving CsI (194.9 mg) in 500 μL DMSO. 48 μL of this cesium solution was added to the 1000 μL $FAMA_{0.22}Pb_{1.1}I_{3.2}Br_{0.66}$ solution, to give the final precursor solution.

Inverse-structure perovskite cells

The inverse-structure perovskite cells were prepared using a modified procedure based on previous reports.[75,78,85,90] The fluorine doped tin oxide (FTO) layer was selectively etched away with Zn dust and 2 M HCl before cleaning the glass slides in a Piranha solution. A 1.0 M nickel oxide precursor solution was prepared by dissolving $Ni(NO_3)_2\cdot6H_2O$ (1.454 g) in 5 mL ethylene glycol and 334 μL ethylenediamine (1.0 M in the final solution).[90] The solution was filtered twice through a 0.20 μm PTFE Millipore Millex-FG filter and spin-coated on the FTO glass slides at 5000 RPM for 45 s. The samples were anealed in two steps, at 373 K for 30 min, and at 573 K for 60 min, to give the NiO_x hole transport layer (HTL). Full details of the NiO_x preparation can be found in Ref. 90 by Hoye et al.

The hot samples were next transferred inside the glovebox for the perovskite and electron transport layer (ETL) deposition. A two-step spin-coating program was employed for the perovskite layer, with an initial spreading at 1000 RPM for 10 s, followed by spinning at 6000 RPM for 35 s. For the 8-pixel and $0.25\,cm^2$ devices, a smooth perovskite film was achieved by dropping 75 μL chloroform onto the spinning sample 7 s before the end of the program, followed by tempering at 373 K for 30-70 min.[78,79,85,90] A [6,6]-Phenyl C_{61} butyric acid methyl ester (PCBM, 99%, Solenne BV) solution in chlorobenzene (CB, $35\,mg\,mL^{-1}$) was stirred at 343 K for 30 min and filtered through a 0.2 μm polytetrafluoroethylene (PTFE) filter before use. The PCBM solution was spin-coated at 3000 RPM for 45 s to form the ETL. 35 μL of a poly(ethylenimine) (PEIE, 5.8 μL) solution in isopropanol (IPA, 1.5 mL) was next spin-coated under ambient conditions (3000 RPM, 30 s), before returning the samples under inert atmosphere for storage. Lastly, a 100 nm silver layer was evaporated to form the electrical contacts of the solar cells. The deposited layers are visible from the magnified cross-section of a $0.25\,cm^2$ inverse-architecture device in Fig. 1a and from its schematic depiction in Fig. 1b. Specific details regarding the preparation of larger devices are given in the Supporting Information.

Field's metal-epoxy encapsulation

To prevent degradation of the perovskite layer by the aqueous electrolyte, a Field's metal-epoxy encapsulation was employed.[11,75] In this case, 0.5-1 mm thick protective foils were obtained by melting the bulk alloy onto a clean hotplate at 363 K and spreading the liquid metal using common glass slides. After cooling below 323 K, the large area foils could be peeled off the hotplate, and cut into the desired dimensions. A small piece of the metal foil was first melted on top of the silver contact, by applying a 2.4 A current for 30 s to a Peltier thermoelectric element, and then solidified by applying –2.4 A for 30 s (2-step chronopotentiometric sequence on a IviumStat instrument). After sealing the edges with Araldite 5-Minute Rapid two component epoxy, the photoelectrodes were stirred in a K_2PtCl_4 (21.4 mg, 51.6 mmol) aqueous solution (5.16 mM, 10 mL) for 20 s and left immersed for a further 40 s, resulting in an electroless deposition of catalytically active Pt nanoparticles on the Field's metal. All encapsulation steps were conducted at ambient conditions.

$BiVO_4$|TiCo photoanodes

$BiVO_4$ photoanodes were prepared similarly to previous reports.[47,91] In case of the $0.25\,cm^2$ devices, a solution was prepared by dissolving $Bi(NO_3)_3\cdot5H_2O$ (0.194 g, 0.4 mmol) and NaI (1.199 g, 8.0 mmol) in Milli-Q water (20 mL). After sonicating with an ultrasonic probe (Fischer Scientific Model 120 Sonic Dismembrator) for 3 min at 100% amplitude, the pH was adjusted to 1.20 using concentrated nitric acid. A second solution consisting of p-benzoquinone (0.292 g, 2.7 mmol, 0.3 M) in absolute ethanol (9 mL) was also sonicated for 3 min. The two solutions were mixed and stirred for 30 min at room temperature to obtain a dark brown BiOI precursor solution. After cleaning the FTO glass slides for 10 min in Piranha solution, and masking the active area with adhesive tape, the orange BiOI layer was electrodeposited onto the active area of the FTO slides, by maintaining a potential of –0.3 V against a Ag/AgCl reference electrode for

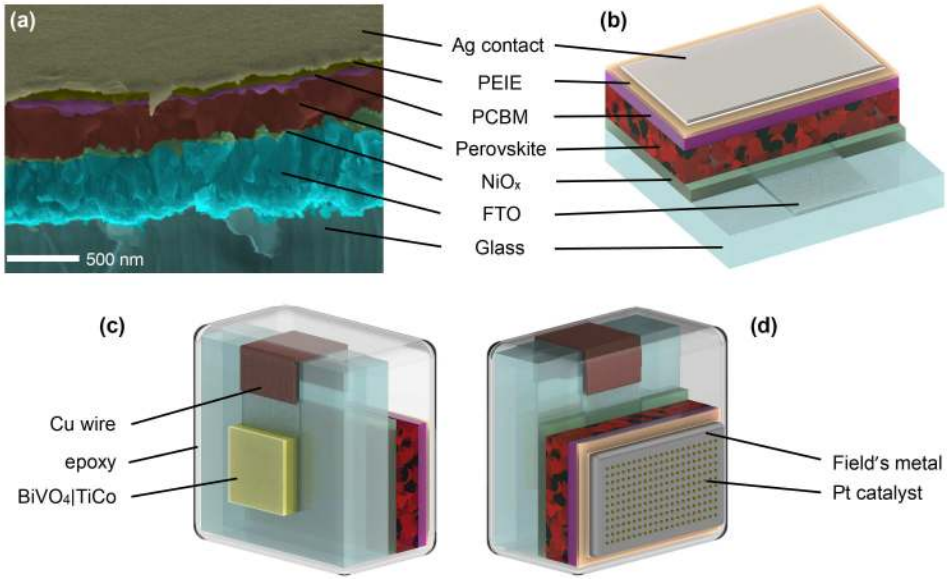

Figure 1 Architecture of the 0.25 cm^2 inverse-structure perovskite cell and of the corresponding photoelectrochemical tandem device. (a) False colour cross plane scanning electron microscopy (SEM) image. (b) Rendering of the photovoltaic cell. (c) Rendering of the PEC tandem cell, as seen from the front side $BiVO_4$ photoanode. (d) Back side view of the rendered PEC tandem, revealing the platinum catalyst deposited onto the Field's metal encapsulation.

5 s, followed by –0.1 V for 180 s. A vanadyl acetylacetonate solution was prepared by sonicating $VO(acac)_2$ (0.530 g, 2.0 mmol) in 5 mL DMSO for 5 min. 40 $\mu L\,cm^{-2}$ of the $VO(acac)_2$ solution was drop-casted onto the BiOI active areas, before heating the glass slides at 723 K for 60 min with a ramp rate of 1 $K\,min^{-1}$. The brownish V_2O_5 crust was dissolved from the photoanode surface by gentle stirring for 30 min in a NaOH (0.2 M) aqueous solution.

A $[Ti_4O(OEt)_{15}(CoCl)]$ (TiCo single source precursor, 0.024 g, 24.5 μmol) solution in dry toluene (5 mL) was prepared under inert atmosphere. 20 $\mu L\,cm^{-2}$ of the single source precursor solution were spin coated four times at 2000 RPM for 10 s under air, to obtain a transparent TiCo catalyst layer.[47] The amount of reagents employed for the preparation of the larger electrodes can be found in the Supporting Information.

Characterisation

Photovoltaic cells The simulated solar irradiation was achieved using a Sun 2000 Solar Simulator (Abet Technologies), which was calibrated to 100 $mW\,cm^{-2}$ (1 sun) using a silicon reference solar cell RS-OD4, and by taking a mismatch factor of 1/1.12 into account. The 8-pixel and 0.25 cm^2 devices were investigated under inert atmosphere using gas-tight sample holders, whereas the IV curves of the larger devices were recorded in their encapsulated form, using the Field's metal as an electrical contact. All devices were characterized without additional masking. The applied potential was varied by a Keithley 2635 source meter, which also recorded the generated current. Reverse and forward IV curves were determined separately between −0.1 and 1.2 V, with a scan rate of 100 $mV\,s^{-1}$. The external quantum efficiency (EQE) of the working devices was determined using a Newport Oriel 66881 setup, an Oriel 74000 Cornerstone monochromator, the Keithley 2635 source meter, a Keithley 2000 multimeter for the Thorlabs SM05PD1A reference photodiodes, a LIA-MV-200-H lock-in-amplifier and a Thorlabs PDA200C photodiode amplifier. The spectra were recorded between 375 and 900 nm, with a 5 nm step size, a 50 ms delay and at 0 V bias.

Photoelectrochemical devices To investigate the performance of the 0.25-4 cm^2 photoelectrodes, a Newport Oriel 67005 solar light simulator was employed with an Air Mass 1.5 Global (AM 1.5G) solar filter. A LOT-QD LS0816-H large area solar simulator was instead used for the 10 cm^2 devices. The light intensity was calibrated to 100 $mW\,cm^{-2}$ (1 sun) using a Newport 1916-R optical power meter. Electrochemical measurements (e.g. cyclic voltammetry, chronoamperometry) were conducted on Ivium CompactStat.e potentiostats, with a sample as the working electrode, a $Ag/AgCl/KCl_{(sat)}$ (Basi) reference electrode and a platinum mesh counter electrode. The electrodes were submerged in a 0.1 M potassium borate buffer (KBi) solution of pH 8.50, which contained 0.1 M K_2SO_4 as supporting electrolyte. In the 3-electrode configuration, the anodic and cathodic compartments were separated by Selemion (AGC Engineering) or Nafion ion exchange membranes for the 0.25 and 1 cm^2 photoelectrodes, respectively. Due to mass transport limitations, the solution was only stirred in case of the photoanodes, and left unstirred otherwise. The cyclic voltammetry measurements were conducted between −0.2 and 1.2 V vs. RHE for the photocathodes, and between 0.1 and 1.4 V vs. RHE for the photoanodes, at a scan rate of 10 $mV\,s^{-1}$. The potential versus RHE was determined using Eq. (1) at a temperature of 298 K.[75]

$$E[V\ vs.\ RHE] = E[V\ vs.\ Ag/AgCl] + 0.059 \times pH + 0.197 \qquad (1)$$

Similar conditions were also employed for the tandem devices, where the scans were conducted in a two electrode configuration, between −0.6 and 1.4 V. To allow ionic movement, a narrow opening was made below the sample instead of using a separating membrane (see Fig. 2). The front $BiVO_4$ active area of the PEC tandems was additionally surrounded by opaque adhesive tape, to prevent any unfiltered light from reaching the perovskite photocathode (see Fig. 2b,c).

The EQE was determined using a LOT MSH-300 monochromator, a Thorlabs PM100D power meter with a Thorlabs S302C thermal power sensor, and an IviumStat potentiostat. The wavelength λ (full width at half maximum of 15 nm) was typically

varied between 300-800 nm in 25 nm steps every 30 s. The resulting EQE was determined using Eq. (2), where h is the Planck constant, c is the speed of light, J is the photocurrent density, e is the electron charge and P_λ is the wavelength-dependent light intensity flux (or irradiance).[92]

$$EQE = \frac{hcJ}{e\lambda P_\lambda} \tag{2}$$

A Shimadzu GC-2010 Plus gas chromatograph (GC) was employed for H_2 evolution measurements. The gas-tight electrochemical cells were purged with nitrogen containing 2% methane as an internal standard. The amount of H_2 was determined by manually injecting 100 μL from the PEC cells' headspace using gas-tight syringes. A NeoFox-GT fluorometer and Fospor-R fluorescence oxygen sensor probes from Ocean Optics were used to determine the amount of produced O_2. The faradaic yield (FY) of the photoelectrodes was determined by comparing the amount of evolved gas (n_{gas}) to the total charge passed (Q), as shown in Eq. (3). The equivalent charge used per gas molecule amounts to $z = 2$ for the H_2 generation, and to $z = 4$ for the O_2 evolution, while F is the Faraday constant.

$$FY = \frac{n_{gas} z F}{Q} \tag{3}$$

The total charge was obtained by integration of the recorded current (I) over the duration (t) of the chronoamperometry. This is illustrated in Eq. (4), where t_0 and t_e represent the beginning and end-points of the measurement.

$$Q = \int_{t_0}^{t_e} I(t)dt \tag{4}$$

Henry's law was employed to compensate for the small effect of dissolved gases,[93] although it is worth noting that the concentration in solution of an evolving gas is probably higher than its equilibrium level.

In order to characterize the performance of tandem devices, the applied bias photon-to-current conversion efficiency (ABPE) was additionally calculated using Eq. (5), where U_{bias} is the applied bias, and P_{total} is the total recorded light intensity flux (100 mW cm^{-2}).[47]

$$ABPE = \frac{J(1.23\ V - U_{bias})}{P_{total}} \tag{5}$$

Similarly, the applied bias solar-to-hydrogen (AB-STH) efficiency can be also calculated as the product of ABPE and FY at a given applied bias (in our case, $U_{bias} = 0$ V).

Statistics The reported values were averaged from the data of at least three PV or PEC devices unless otherwise noted. The given errors correspond to the calculated standard deviation. Examples of typical data are taken from stable devices which follow the general trend, having around or above average performance.

Materials An FEI sFEG XL30 scanning electron microscope (SEM) was employed to investigate the surface and cross-plane topology of the devices. Energy-dispersive X-ray (EDX) spectra were recorded using an Oxford Instruments X-Max silicon drift detector to confirm the elemental composition of various samples. The formation of the polycrystalline perovskite phase was confirmed by X-ray powder diffraction (XRD) measurements, which were conducted on a Panalytical Empyrean X-ray diffractometer. The spectra were recorded using Cu Kα radiation, in a θ–2θ configuration. The angle of the incident beam was varied between 10° to 90° with a step size of 0.008. The thin film samples were rotated at a speed of 30 RPM.

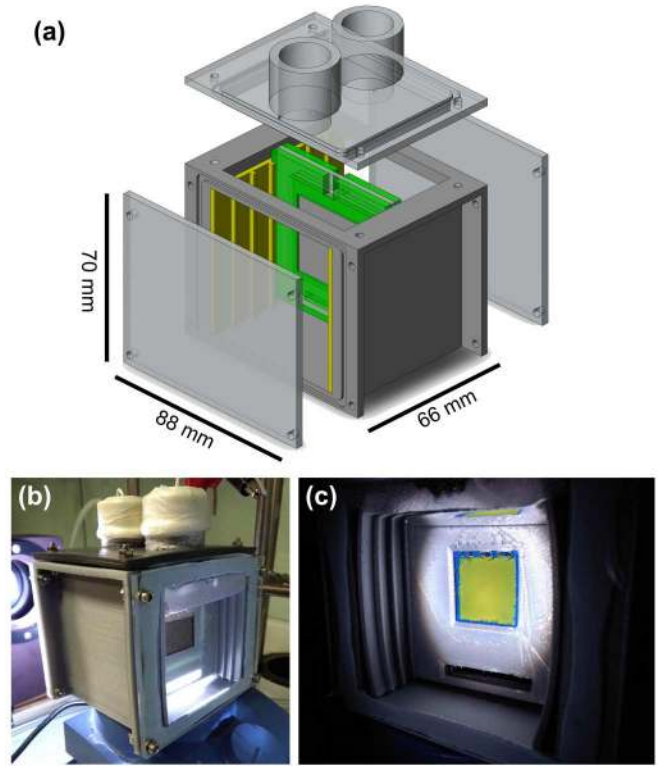

Figure 2 Various representations of the modular 3D-printed PEC cell. (a) 3D rendering of the cell's components, revealing the removable sample holder (depicted in green), which can slot in along the exchangeable side rails (yellow). (b) Back side view of the PEC cell under use for tandem characterisation, with the Field's metal - Pt nanoparticle interface exposed to the electrolyte solution. (c) Front side view of the anodic compartment, showing the $BiVO_4$|TiCo photoanode of a 4 cm^2 tandem under 1 sun irradiation.

3D-printed PEC cell

Common glass PEC H-cells with membrane separation were employed for the characterisation of 0.25 and 1 cm^2 photoelectrodes (see Ref. 75 and Supplementary Video). A 3D-printed cell was developed for the larger electrodes and all back-to-back tandems, to maintain a constant sample position and ensure a certain separation between the cathodic and anodic compartments. In comparison to other recent models which have employed 3D-printing for electrodes,[94–96] electrochemical flow reactors[97–100] or biased photoelectrodes,[101] this represents the first reported 3D-printed PEC cell design for bias-free tandems.

While existing (mainly glass) PEC cell models are often made to accommodate samples of fixed dimensions, our modular design provides a facile way to measure samples of different sizes in various configurations (i.e. 3-electrode, monolithic, wired, or even colloidal systems). For this purpose, replaceable sample holders are employed which can slide along the side rails. The holders cover the non-active area of the devices, to prevent additional unfiltered light from reaching the back-side of the tandems. The working principle is illustrated by the 3D model in Fig. 2a, where the thin slides supporting the sample are highlighted in green and the lateral rails are depicted in yellow. Photographs of the 3D-printed PEC cell during use can be also found in Fig. 2b and c, revealing the back- and front-side of a 4 cm^2 tandem, respectively.

In order to obtain a light-weight, inexpensive, and easily adjustable PEC cell, the 3D components were designed in SolidWorks, and created from polylactic acid (PLA) using an Ulti-

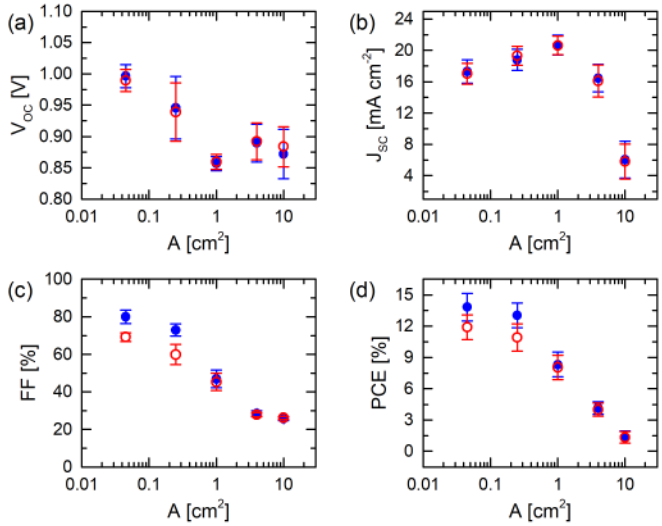

Figure 3 Dependence of the photovoltaic parameters of the perovskite devices on their photoactive area: (a) open circuit voltage (V_{OC}), (b) short circuit current density (J_{SC}), (c) fill factor (FF), and (d) photovoltaic cell efficiency (PCE). The average data of backward and forward scans is indicated by blue dots and red circles, respectively.

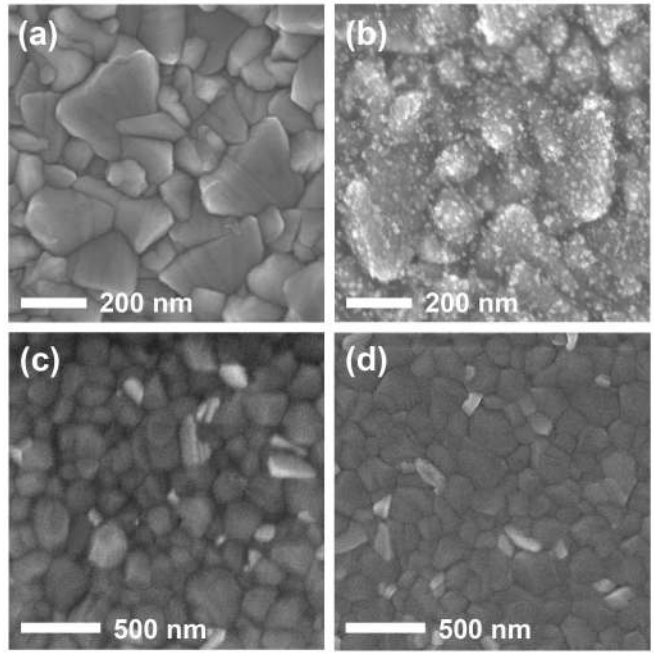

Figure 4 SEM images revealing the NiO_x-induced morphological changes for the perovskite samples. (a) Bare FTO substrate. (b) Complete coverage of the FTO grains by a thin NiO_x film. (c) Top view of a perovskite layer, which is spin-coated on bare FTO. (d) Top view of a perovskite layer deposited onto FTO|NiO_x. The NiO_x forms a pinhole-free coating of the rough FTO grains, resulting in homogeneous perovskite crystallisation.

maker 2 Extended+ 3D printer. Sketches of the main components and their assembly are given in Fig. S1 from the Supporting Information. The PEC cell's windows consisted of 3 mm thick Perspex® acrylic glass, whereas Blu Tack reusable adhesive was used as a sealant.

3 Results and discussion

3.1 Perovskite photovoltaic cells

A NiO_x hole transport layer [90] was deposited on top of the FTO coated glass substrate by spin-coating a $Ni(NO_3)_2 \cdot 6H_2O$ precursor solution followed by annealing. A state-of-the-art cesium formamidinium methylammonium (CsFAMA) triple cation perovskite photoabsorber was deposited by spin-coating using the established anti-solvent method. [78,79,85,90] PEIE [102] was spin-coated on top of the thin PCBM electron selective layer, to prevent interfacial degradation [103] from the reaction of silver with the halide ions. The additional physical separation provided by the PEIE layer is noticeable when comparing Fig. 1a of a complete device with Fig. S7a (Supporting Information) of the bare PCBM on a perovskite substrate. This design provided a performance improvement over our previously reported devices, [75] where a PEDOT:PSS HTL and a $MAPbI_3$ photoabsorber were used.

To draw an accurate comparison between the performance of a photocathode and the underlying photovoltaic component, all devices have been first investigated as solar cells. In this way, thorough batch statistics of the photocathodes could be made, by taking already faulty PV devices into account.

The average photovoltaic parameters are depicted as a function of the device area in Figure 3, with the exact values given in Table 1. The corresponding histograms for the 0.045, 0.25 and 1 cm^2 devices can be found in Figures S2-S6 from the Supporting Information. Examples of typical IV curves are also presented in Figure 6a.

In general, the small 8-pixel devices (area 0.045 cm^2) present the best performance, with the champion device reaching an efficiency of 16.4% in backward scan direction, with an open circuit voltage (V_{OC}) of 0.99 V, a short circuit current density (J_{SC}) of 19.7 mA cm^{-2} and a fill factor (FF) of 83.1%. The improved V_{OC} of 1.00±0.02 V is also consistent with previous reports, which indicate a better alignment between the work function of NiO_x and the perovskite's valence band edge level than in the case of PEDOT:PSS, which typically only delivers V_{OC} values between 0.5-0.9 V. [104–108]

As observed from Figure 3d, a roughly logarithmic decrease in the photovoltaic cell efficiency (PCE) with the active area occurs above a surface of 0.25 cm^2, due to resistive losses. [109,110] These losses manifest mainly through a decrease in the fill factor (see Figures 3c and 6a), which induces a similar behaviour in the J_{SC} (Figure 3b). This leads to a limitation of the maximum short circuit current below 100 mA, as observed for the 4 and 10 cm^2 devices. The less pronounced decrease in the V_{OC} (Figure 3a) may be due to an increasing shunt resistance originating from more defects and pin-holes in the layer structure of the larger devices. Nevertheless, our study on the scalability of single pixel perovskite PV cells (as opposed to serially connected modules) reveals that efficiencies above 1% can be obtained even for 10 cm^2 devices, whereas the Field's metal is also first demonstrated as a valid encapsulant for photovoltaic applications. These observations indicate that metal fingers at distances between 0.5-1 cm from each other are required for maintaining a high performance in large scale perovskite applications, similar to the ones available for silicon panels.

Another interesting aspect of our findings is that the NiO_x layer (Figure 4b) can also effectively cover the rougher surface of bare FTO (4a). In this case, a very thin coating of NiO_x nanoclusters is formed, which does not present additional peaks in the XRD spectra (Figure S8, Supporting Information). This smoothing of the underlying surface appears to result in more homogeneous and better packed perovskite grains (Fig. 4c,d). While the higher surface roughness of FTO has made indium tin oxide (ITO) glass the preferred choice for planar inverse-structure per-

Table 1 Numerical data of the photovoltaic parameters illustrated in Figure 3. The open circuit voltage, short circuit current density, fill factor and photovoltaic cell efficiency are given as a function of the photoactive area for both forward (f) and backward (b) scans, whereas the number of working devices from the total amount produced is also shown.

Area [cm^2]	$V_{OC,b}$ [V]	$J_{SC,b}$ [$mA\,cm^{-2}$]	FF_b [%]	PCE_b [%]	$V_{OC,f}$ [V]	$J_{SC,f}$ [$mA\,cm^{-2}$]	FF_f [%]	PCE_f [%]	Devices working (total)
0.045	1.00±0.02	17.3±1.5	80.0±3.6	13.8±1.3	0.99±0.02	17.0±1.3	69.2±2.3	11.9±1.2	47(48)
0.25	0.95±0.05	18.8±1.4	72.9±3.2	13.0±1.2	0.94±0.05	19.3±1.2	59.8±5.4	10.9±1.3	22(24)
1	0.86±0.01	20.7±1.3	46.9±4.7	8.3±1.2	0.86±0.01	20.6±1.2	45.3±4.7	8.0±1.2	10(12)
4	0.89±0.03	16.5±1.7	28.4±1.5	4.2±0.6	0.89±0.03	16.1±2.1	27.8±1.2	4.0±0.6	6(6)
10	0.87±0.04	6.1±2.4	25.6±0.9	1.36±0.58	0.88±0.03	5.8±2.2	26.2±0.8	1.35±0.54	6(6)

ovskite cells,[111,112] these results show that the former can be also successfully employed. Since FTO is chemically more robust to aggressive cleaning methods (e.g. Piranha solution) and has a typically lower sheet resistance, its use has a potential advantage for large scale, industrial applications.

3.2 Perovskite-based photocathodes

After the photovoltaic characterisation, the 0.25 cm^2 perovskite PV devices (abbreviated PVK) were encapsulated by briefly melting a thin Field's metal (FM) sheet on top of the silver contact via a Peltier thermoelectric element and sealing the edges with epoxy resin. By maintaining the Field's metal in a liquid state for only 20-40 s, a good adhesion to the underlying silver contact was ensured, while preventing a degradation of the perovskite layer through exfoliation of the Ag layer. Following the electroless Pt nanoparticle deposition, the performance of the resulting PVK|FM|Pt photocathodes was investigated for H_2 evolution. Typical examples of the results are depicted in Figure 5a,b, where the sign of the photocathode traces is reversed for convenience. Further data from all devices can be found in Figures S16-S18 from the Supporting Information.

In order to determine the reliability of the device fabrication procedures, performance statistics have been performed on an initial batch of eight 0.25 cm^2 PV devices ($V_{OC,b}$ 1.00±0.06 V, $J_{SC,b}$ 18.9±0.8 $mA\,cm^{-2}$, FF_b 72.3±3.8%, PCE_b 13.7±0.9%), from which two were shorted. Due to the improved encapsulation technique using thin Field's metal foils and a Peltier thermoelectric element, all six remaining devices could be investigated for photoelectrochemical studies.

While the favourable position of the NiO_x energy levels provide an improvement of around 0.1 V in the V_{OC} of the PV devices, a slightly more negative onset potential of around 0.6-0.8 V vs. RHE was obtained for all photocathodes as compared to the previous 0.95±0.03 V vs. RHE.[75] However, the use of the CsFAMA triple cation perovskite resulted here in an almost doubling of the photocurrent over our initial $MAPbI_3$ devices,[75] with 5 out of 6 samples delivering an average value of –12.1±0.3 $mA\,cm^{-2}$ at 0 V vs. RHE (see Fig. 5a, red curves, and Fig. S16 from the Supporting Information). This high current density is compatible with state-of-the-art PV-electrolyser and PV-PEC systems which reach between 4-12 $mA\,cm^{-2}$ under bias-free conditions.[21,39,40,53,65] Thus the encapsulated perovskite photocathodes are valid alternatives to existing components in the wired designs for solar fuel generation. Moreover, by replacing the acidic, hydrophilic PEDOT:PSS HTL[111–113] with the robust NiO_x,[90,106,107] a significant improvement in the device stability has been obtained from the initial 1-2 h,[75] with 4 out of 6 devices lasting for at least 4 h under use (up to 7 h stability for our champion device, see Figures 5b and S16 from the Supporting Information). For those devices, the average faradaic yield (FY) amounted to 78.8±3.5% after 4 h. Losses are possibly caused by the entrapment of small H_2 bubbles along the measuring cell's glass walls or by leakage due to overpressure in the cathodic compartment.

Similar results have also been recorded for four 1 cm^2 PV devices ($V_{OC,b}$ 0.867±0.002 V, $J_{SC,b}$ 21.1±1.3 $mA\,cm^{-2}$, FF_b 50.2±4.7%, PCE_b 9.2±1.2%, no shorted cells). In this case, a comparable average photocurrent of –9.3±1.1 $mA\,cm^{-2}$ at 0 V vs. RHE was determined for all four corresponding photocathodes, and the more noisy voltammetric signal was likely caused by the vigorous hydrogen evolution (see Fig. S17 and Supplementary Video). Two devices lasted beyond 2 h (FY 74.7±3.0%, see Figure S17 from the Supporting Information), with the slight loss in stability due to a higher probability of water leakage with increasing area, combined with additional mechanical stress during the transport of the encapsulated devices for PV characterisation.

3.3 $BiVO_4$|TiCo photoanodes

The $BiVO_4$|TiCo photoanodes of corresponding sizes were prepared similarly to reported procedures.[47,91] BiOI was electrodeposited onto FTO glass and annealed in the presence of a vanadium precursor. The TiCo catalyst was spin-coated from a single source precursor solution.[47]

A photoelectrochemical batch analysis has also been conducted for the $BiVO_4$|TiCo photoanodes, with results for all devices presented in Figures S19-S21 from the Supporting Information and typical linear sweep voltammetry (LSV) scans depicted in Figure 5a (blue curves). For a batch of six 0.25 cm^2 devices, the average photocurrent density amounted to 1.61±0.28 $mA\,cm^{-2}$ at an applied potential of 1.23 V vs. RHE (see Figure S19, Supporting Information), whereas it reached 1.31±0.10 $mA\,cm^{-2}$ at 1.23 V vs. RHE for three 1 cm^2 devices (Figure S20, Supporting Information).

Since the comparatively high stability of $BiVO_4$ under use is well known,[114–117] the chronoamperometric measurements at 1.23 V vs. RHE have only been conducted for 4 h, to match the stability of the perovskite-based photocathodes. An example is given in Figure S12 (Supporting Information), which also reveals the corresponding amount of oxygen detected by the fluorescence sensor after subtraction of the initial background leakage (see Figures S19 and S20 for the linear fitting of the raw fluorescence lifetime τ signals, and Scheme S2 for a clarification on the extracted information, Supporting Information). The resulting faradaic yield only amounted to 38.4±10.7% for the 0.25 cm^2 devices, due to the particular affinity of the O_2 bubbles to the glass walls of the measuring cells. The oxygen-glass affinity also explains why a slow equilibrium is reached after the end of the chronoamperometry, since the oxygen needs to first dissolve from the bubbles into the solution, then diffuse to the upper gas space (Figure S12, Supporting Information). A similar value of 31.2±9.2% was obtained for the 1 cm^2 devices.

3.4 Perovskite-$BiVO_4$|TiCo PEC tandem devices

For the tandem systems, a back-to-back configuration has been preferred over a wired PEC design due to several reasons. The

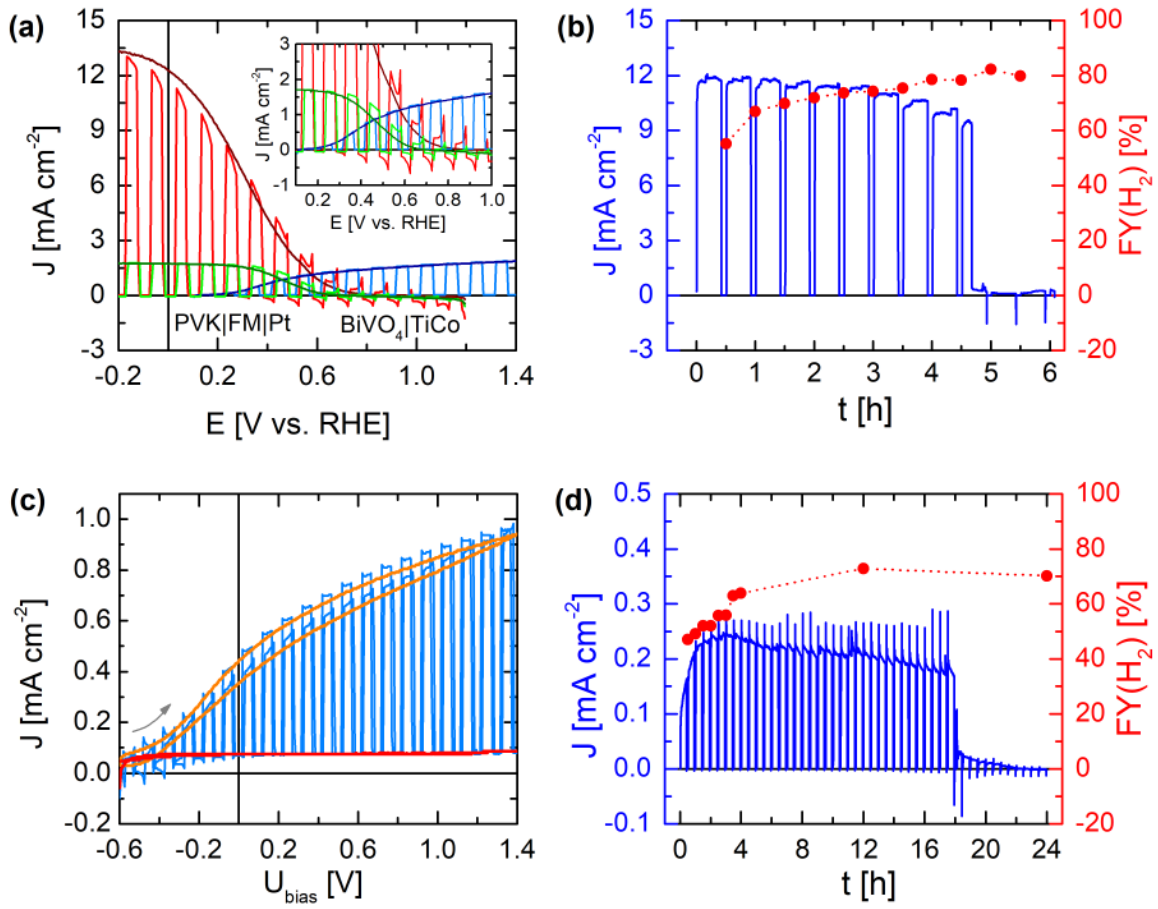

Figure 5 Typical data recorded for the 0.25 cm^2 PEC devices (irradiation provided by a solar light simulator, 100 mW cm^{-2}, AM 1.5G). (a) Comparison between the continuous and chopped light linear sweep voltammograms in 3-electrode setup of a $BiVO_4$|TiCo photoanode (blue shades), a perovskite-based photocathode (red tones), and the photocathode in tandem configuration with $BiVO_4$|TiCo light filtering (green) (scan rates 10 mV s^{-1}, in the direction of photocurrent increase). The sign of the reductive currents is reversed for convenience. (b) Chronoamperometric trace of the H_2 evolution current for a perovskite-based photocathode at 0 V vs. RHE and corresponding faradaic yield. (c) Light, dark and chopped cyclic voltammetry scans of a perovskite-$BiVO_4$|TiCo back-to-back PEC tandem device (scan rate 10 mV s^{-1}, gray arrow indicates starting point and direction). (d) Chronoamperometric trace of the H_2 evolution current and H_2 faradaic yield for a tandem device at no applied bias. For the stability tests, light is switched on for 25 min intervals with 5 min in between, to test for changes in the dark current.

back-to-back monolithic design is closer to the idealized artificial leaf and also provides sufficient spacial separation between the H_2 and O_2 evolution sites. Thus diffusion of the produced oxygen to the cathodic compartment and its subsequent reduction is less likely even in the absence of an ion exchange membrane. High performing $BiVO_4$ photoanodes are designed to maximise scattering.[91,117–120] Therefore, the small gap between the $BiVO_4$|TiCo front side and the perovskite back side ensures that most of the scattered light actually reaches the perovskite photoactive area. The use of 3D printed sample holders of custom size also ensures that no additional scattered light reaches the perovskite component (i.e. by circumventing the $BiVO_4$ active area).

Examples of typical cyclic voltammetry scans and long term stability tests of the 0.25 cm^2 photoelectrochemical tandems are found in Fig. 5c and Fig. 5d, respectively. The data for all tandems can be found in Figures S22-S25 from the Supporting Information.

As seen from Figure 5c, using the $BiVO_4$|TiCo photoanode enables the first example of a bias-free water splitting PEC tandem with an inverse-structure perovskite-based photocathode. Four of the five 0.25 cm^2 devices investigated present an average photocurrent density of 0.39±0.15 mA cm^{-2} at zero applied potential bias (see Fig. S22, Supporting Information). This corresponds to a bias-free photon-to-current efficiency of 0.49±0.18%, which lies close to the maximum achieved at around 0.2 V (see the calculated ABPE curve from Figure S13 in the Supporting Information). The onset potential for water splitting lies around –0.6 V, the most negative reported for photoelectrochemical devices, which means that the tandems can provide enough driving force for simultaneous solar fuel and electricity production. The tandem devices possess an excellent stability of up to 20 h (see Figure S23a of a 1 cm^2 device, Supporting Information), with an average faradaic yield towards hydrogen production of 71.4±13.0% after 12 h. The slower increase in the FY value may be caused by the larger volume of the 3D-printed PEC cell and the textured nature of its PLA walls, which favours gas leakage and the entrapment of bubbles for the smaller samples even more. Accordingly, the solar-to-hydrogen conversion efficiency of the devices amounts to 0.35±0.14%.

The $BiVO_4$ light filtering and scattering is responsible for a lower perovskite photocathode response of –1.73 mA cm^{-2} at 0 V vs. RHE, as exemplified in Fig. 5a (green curves). This shifts the intersect between the perovskite and $BiVO_4$|TiCo photosignals (i.e. the ideal bias-free photocurrent) from 1.13 mA cm^{-2} to 0.85 mA cm^{-2}. Assuming ideal conditions (100% FY, no ohmic

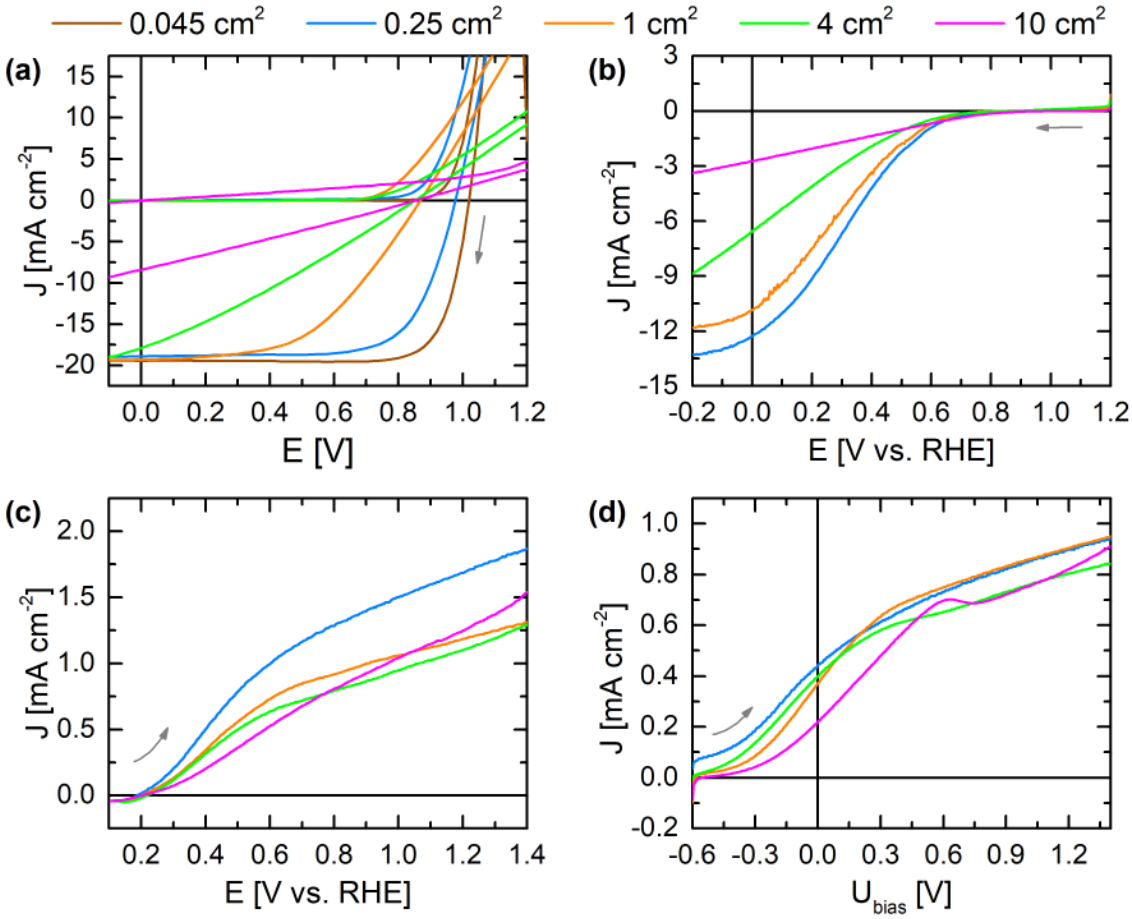

Figure 6 Typical photocurrents observed for the photovoltaic and photoelectrochemical devices of areas between 0.045 and 10 cm^2 (100 mW cm^{-2}, AM 1.5G): (a) PV cells, (b) perovskite-based photocathodes, (c) $BiVO_4$|TiCo photoanodes, (d) perovskite-$BiVO_4$|TiCo PEC tandems (scan rates 100 mV s^{-1} for the PV cells and 10 mV s^{-1} for the PEC devices, gray arrows indicate starting points and direction).

or optical losses), the bias-free 0.85 mA cm^{-2} would correspond to a STH efficiency of 1.05%.

The 1 cm^2 devices (Figure S23, Supporting Information) reached a similar bias-free photocurrent density of 0.43±0.08 mA cm^{-2}, corresponding to a photon-to-current efficiency of 0.53±0.10% and an STH efficiency of 0.37±0.08%. Three out of the four investigated devices delivered an average hydrogen faradaic yield of 69.9±5.2% within 12 h.

The excellent stability of the tandem devices also gives a hint towards the degradation pathways. Since the back side of the electrodes is completely sealed by epoxy resin in the back-to-back configuration, this suggests that water is infiltrating the encapsulated devices from the glass/epoxy interface. Another explanation for the improved stability may be found in the lower photocurrent density, which allows the gases to diffuse away from the electrode surface without vigorous bubbling. The gas bubble formation may also affect the stability of the Field's metal/epoxy interface, as observed from a decreased stability when purging the measuring cell with the perovskite photocathodes immersed in solution.

3.5 Scalability studies

In order to test the scalability of the PEC tandems and corresponding photoelectrodes beyond the commonly reported sizes of up to 1 cm^2, [21,48,65,117] larger devices of 4 and 10 cm^2 were also prepared using the same deposition techniques (see Supporting Information for particular fabrication details). All larger devices were characterised within the 3D-printed PEC cell, in either a 2- or 3-electrode configuration. A comparison of typical photocurrents is found in Fig. 6 for the PV and PEC devices of various sizes. The raw data recorded for the perovskite-based photocathodes, $BiVO_4$|TiCo photoanodes, and PEC tandems can be found in Figures S16-S18, S19-S21, and S22-S25 (Supporting Information), respectively.

The photocurrent response of the perovskite photocathodes follows a decreasing trend similar to the one observed for the PV components in respect to their size (Figure 6a and 6b). As with the efficiency of the photovoltaic cells (Fig. 3), the absolute value of the photocathode current density at 0 V vs. RHE decreases exponentially with the photoactive area (Fig. S11a, Supporting Information), reaching only –2.68±0.80 mA cm^{-2} for the 10 cm^2 devices (22% of the 0.25 cm^2 photocathodes' signal). The photocathodes also show a lower fill factor than the PV cells, due to a combination of the series resistance with the solution resistance and the electrochemical overpotential for H_2 evolution.

While the photocurrent density of the $BiVO_4$|TiCo electrodes is lower than that of their perovskite counterparts in the 3-electrode configuration, the former appear to scale up better, with values stabilising around 1.2-1.4 mA cm^{-2} at 1.23 V vs. RHE for the backside irradiated photoanodes (see Figure 6c and S11b, Supporting Information). The finding is consistent to previous reports, [117,121] which indicate that higher photocurrents are obtained when irradiating a small area. This observation may be explained by a higher overall homogeneity for larger devices (see higher error bar for the 0.25 cm^2 photoanodes, Fig. S11b, Supporting Information), as well as by lower kinetic limitations

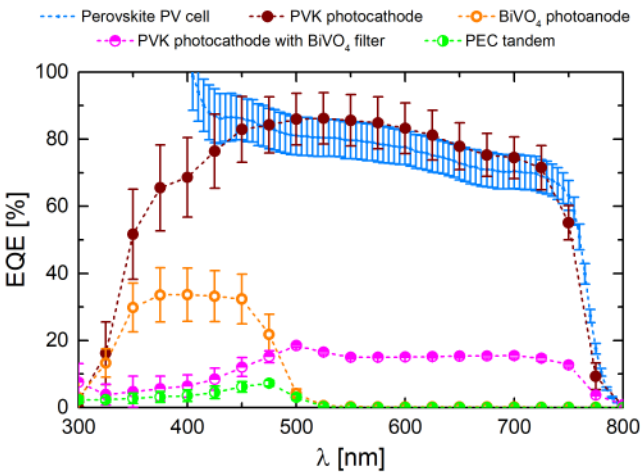

Figure 7 Comparison between the EQE spectra of the various light absorbers, employed for both 0.25 cm^2 solar cells and photoelectrodes. The perovskite photovoltaic cells are investigated at short circuit conditions (0 V). The measurements are conducted at applied biases of 0 V vs. RHE for the perovskite-based photocathodes, 1.23 V vs. RHE for the $BiVO_4$|TiCo photoanodes and 0 V for the perovskite-$BiVO_4$|TiCo PEC tandems.

through ionic diffusion to the electrode surface.[122] The influence of the mass transport limitations on the shape of the cyclic voltammograms and absolute photocurrents are clearly visible from Fig. S14, which compares the voltammetric traces recorded in a stagnant solution to the ones under stirring. Accordingly, we report all PEC characterisation of the individual $BiVO_4$|TiCo photoanodes under stirring.

The perovskite-$BiVO_4$|TiCo PEC tandems also demonstrated a remarkable scalability, as shown by the roughly similar bias-free photocurrents of 0.2-0.5 mA cm^{-2} plotted in Figure 6d. However, a combination of greater series resistance and mass transport limitations have an increasing impact especially for the 10 cm^2 devices, which present a lower bias-free photocurrent of 0.23±0.10 mA cm^{-2} (Figs. 6d and S11c, Supporting Information) and a current peak around 0.6 V (Figs. 6d and S25). While the $BiVO_4$ performance commonly depends on the irradiated side, the back-to-back tandems with front-side irradiated $BiVO_4$|TiCo still present similar photocurrents to the ones of the characterised photoanodes (≈0.8 mA cm^{-2} at 0.9 V applied bias, a close estimate of 1.23 V vs. RHE). Nevertheless, the low transparency of Perspex® acrylic glass at wavelengths below roughly 380 nm (see Fig. S10) may also explain the lower photocurrents.

Due to a higher probability of defects and pin-holes in the perovskite deposition, Field's metal film, or epoxy encapsulation, the larger area devices presented a lower stability in use, which only reached up to 6 h and 14 h for the 4 and 10 cm^2 tandems, respectively (see Figs. S24, S25 from the Supporting Information). Nevertheless, the results obtained for our handmade devices remain very promising, showing potential for further stability improvements in an automated fabrication process.

3.6 External quantum efficiency (EQE) spectra

To gain a deeper insight on the processes influencing the light conversion to fuel, EQE spectra are also recorded for both photovoltaic and photoelectrocatalytic components with the averaged results given in Figure 7. The spectra are recorded at applied biases of 0 V for the perovskite PV cells, 0 V vs. RHE for the perovskite photocathodes, 1.23 V vs. RHE for the $BiVO_4$|TiCo photoanodes, and 0 V for the PEC tandems. As expected, the average EQE spectrum of the six 0.25 cm^2 $BiVO_4$|TiCo plateaus around 30% at wavelengths below 500 nm, whereas the perovskite PV cells harvest light with an efficiency around 80% over the entire visible range (the upwards drift in the lower wavelength region is due to instrumental limitations). The integrated photocurrents obtained from the EQE spectra amount to 1.66±0.44 mA cm^{-2} at 1.23 V vs. RHE and -18.8±1.3 mA cm^{-2} at short circuit conditions, respectively, which are consistent to the IV data obtained under 1 sun irradiation.

Surprisingly, the EQE spectrum of the perovskite-based photocathodes was similar to that of the underlying solar cells. Its integration results in an ideal J_{SC} of –19.3±1.9 mA cm^{-2} at 0 V vs. RHE, which differs significantly from the –12.1±0.3 mA cm^{-2} recorded by cyclic voltammetry. This indicates that the maximal performance of the photocathodes is limited by kinetic effects, namely the fast depletion of protons and the vigorous formation of bubbles in the vicinity of the electrode surface, which decreases the active electrochemical area and inhibits a fast diffusion of protons from within the solution. The finding is consistent to reports of similar limitations in $BiVO_4$ photoanodes[122] and water splitting systems.[123] The mass transport limitation is also observable when recording the cyclic voltammograms in a 0.1 M potassium borate buffer (pH 8.50) without the 0.1 M K_2SO_4 electrolyte salt, as shown in Figure S15 from the Supporting Information. This observation also contributes towards explaining why the performance of various wired perovskite-based systems[53,55–57,72,124] is similar regardless of their photovoltaic efficiency, since the concentration and nature of the electrolyte solution actually plays the major limiting role.

3.7 Comparison with state-of-the-art and outlook

Overall, these findings reveal the scalability of the perovskite-$BiVO_4$|TiCo photoelectrochemical tandem devices. While the STH efficiency of around 0.3% is lower than the 2-6% reported for PV and PEC multijunction systems (i.e. overall ≥3 photoabsorbers),[21,22,57,123] its value compares favourably to state-of-the-art devices containing oxide-,[45,125] or single-junction silicon-photocathodes.[47,48,50,126] Moreover, the stability reaching 20 h and scalability of up to 10 cm^2 presented in this work counts among the highest reported values, even surpassing most PV-PEC and wired systems (see Table 2 for a detailed literature comparison), which emphasizes the relevance of our findings as an early step towards commercial implementation.

From this point of view, a lower bias-free photocurrent can even prove beneficial for commercial systems by preventing bubble formation.[127] In this case, the dissolved gas could be removed from the PEC cell and separated in a recirculating system, which can be powered by the additional driving force of up to 0.6 V of the tandems. To mitigate the effect of device degradation and resistive losses on the overall performance of such assemblies, a tiled design consisting of smaller wireless tandems could be constructed, where any faulty device could be simply replaced. For larger tandem devices, the lateral resistive losses caused by the FTO sheets[128,129] may be again avoided by introducing metal fingers.[130] In those cases, the total footprint area of the module would also need to be taken into account.[57,86] Alternatively, a low temperature HTL[131–133] and $BiVO_4$[134,135] deposition on flexible, thin-film substrates[136–138] would provide further commercial advantages, by obtaining lighter devices which may be mass-produced by scalable roll-to-roll techniques.[86,89] Concerning the device encasing, modular designs similar to the one presented here could be easily scaled-up.

Beyond the practical side, the facile 3D-printed design could also enable widespread research on solar fuels in developing

Table 2 Comparison between our results and several state-of-the-art PEC, PV-PEC and PV-electrolyser water splitting devices. Data is reported under 1 sun simulated irradiation (100 mW cm^{-2}, AM 1.5G). [a]FY after 12 h. [b]FY after 1 h. [c]Assumed value. [d]Electrolyte: 0.5 M KBi, 1.5 M KNO_3.

Tandems	J_{0V} [mA cm^{-2}]	FY [%]	STH [%]	Stability [h]	Area [cm^2]	Electrolyte solution	Reference
PEC							
PVK|FM|Pt–$BiVO_4$|TiCo	0.39±0.15	71.4±13.0[a]	0.35±0.14	18	0.25	0.1 M KBi, K_2SO_4 (pH 8.50)	this work
PVK|FM|Pt–$BiVO_4$|TiCo	0.43±0.08	69.9±5.2[a]	0.37±0.08	20	1	0.1 M KBi, K_2SO_4 (pH 8.50)	this work
PVK|FM|Pt–$BiVO_4$|TiCo	0.43±0.04	46.2±4.5[b]	0.25±0.03	6	4	0.1 M KBi, K_2SO_4 (pH 8.50)	this work
PVK|FM|Pt–$BiVO_4$|TiCo	0.23±0.10	52.2±5.3[b]	0.15±0.06	14	10	0.1 M KBi, K_2SO_4 (pH 8.50)	this work
Au|Cu_2O|Al:ZnO|TiO_2|RuO_x–$BiVO_4$|Co-Pi	0.318	-	< 0.5	1.4	0.283	0.5 M Na_2SO_4, 0.09 M KH_2PO_4, 0.01 M K_2HPO_4 (pH 6)	45
p-Si|TiNi–$BiVO_4$|TiCo	0.045±0.018	91±5.3	0.05	24	0.5-4	0.1 M Bi, K_2SO_4 (pH 9.2)	47
p-Si|TiO_2|(Fe_2O_3 csh-NW)–TiO_2/TiO_2 cs-NT	≈0.15	100[c]	≈0.18	-	-	NaPi, 0.25 M Na_2SO_4 (pH 7.1)	50
p-Si nanoarray|Pt–Mo:$BiVO_4$|Co-Pi	0.46	100[c]	0.57	3.5	0.28	0.1 M KPi (pH 5.5)	48
PV–PEC							
DSC–WO_3	2.52	≈100	3.10	≈9	0.2	1 M $HClO_4$ (pH 0)	28
DSSC–WO_3/W,Mo:$BiVO_4$|FeOOH/NiOOH	4.7	≈100	5.7	12	≈0.3	0.1 M NaPi (pH 6.9)	32
(1-jn a-Si)–W:$BiVO_4$|Co-Pi	3	100[c]	3.6	1	1	0.1 M KPi (pH ≈7.3)	21
PVK–Mo:$BiVO_4$|Co-Ci (wireless)	≈3.5 (-)	≈100	4.3 (3)	12	0.42 (1.3)	0.1 M $KHCO_3$ (pH ≈7)	61
PVK–Mo:$BiVO_4$|Fe(Ni)OOH	5.01	≈92	6.2	10	0.25	0.5 M KH_2PO_4 (pH 7)	65
multi-jn PV – PEC							
(2-jn a-Si)–W:$BiVO_4$|Co-Pi	4	100[c]	4.9	1	0.38	0.1 M KPi (pH ≈7.3)	21
(a-Si:H/nc-Si:H)–W:$BiVO_4$|Co-Pi	4.22	100[c]	5.2	1	1	0.1 M KPi (pH ≈7)	22
(multi-jn) PV – electrolyser							
a-Si:H/a-Si:H|ZnO:Al|Ag|Pt–RuO_2	3	100[c]	6.8	50	0.5	0.1 M H_2SO_4	39
(2-serial PVK)–NiFe LDH	10	100	12.3	4	0.318	1 M NaOH	53
(2-serial PVK)–CoP, NiFe LDH	10.35	100	12.7	16	0.32	0.5 M H_2SO_4 | 1 M KOH	55
Co|3jn-a-Si|NiMoZn wireless	-	≈100	2.5[d]	32	2	1 M KBi (pH 9.2)	123
(3-serial PVK)–CP|N-CNT|$NiCo_2O_4$	≈5	100	6.2	0.5	0.12	0.1 M KOH (pH 13)	57

countries, since the raw materials (PLA, Blu Tack, acrylic glass) cost only a fraction of the price of highly specialised commercial PEC cells. Accordingly, a few national 3D-printing workshops could provide small- and medium-scale reactors for local laboratories, bringing this fundamental science closer to the communities most in need.

4 Conclusions

In conclusion, we have investigated the potential of using perovskite-$BiVO_4$ photoelectrochemical tandems for bias-free solar water splitting. By employing the CsFAMA triple cation mixed halide perovskite as the photoabsorber and NiO_x as the hole selective layer, substantial improvements have been achieved in the performance (–12.1±0.3 mA cm^{-2} at 0 V vs. RHE) and stability (up to 7 h) of 0.25 cm^2 photocathodes, with the corresponding PV devices reaching an efficiency of 13.0±1.2%. The 1 cm^2 back-to-back PEC tandems presented a remarkable stability of up to 20 h for the bias-free water splitting, with a corresponding solar-to-hydrogen conversion efficiency of 0.37±0.08%. Their very negative onset bias of around –0.6 V enables simultaneous solar fuel and electricity production, providing also flexibility for either operation mode.

Due to significant progress in production techniques, an excellent reproducibility and reliability have been obtained for both single pixel solar cells and photoelectrodes. Those advantages enabled a further comprehensive study on the device up-scaling from 0.25 to 10 cm^2, which revealed valuable insights into the resistive and kinetic limitations affecting both photovoltaics and photoelectrocatalysis. The excellent scalability of our perovskite and $BiVO_4$ electrodes allowed us to obtain a comparable activity for 10 cm^2 PEC tandems, which are to the best of our knowledge the largest reported devices of their kind. To characterize the performance of the larger bias-free PEC tandems, an affordable 3D-printed measuring cell was also designed for the first time, which may be easily adjusted for laboratory research or consumer-based applications.

Our results reveal that encapsulated perovskite photocathodes and the corresponding photoelectrochemical tandems can compete in terms of stability and scalability with more established PV-PEC or PV-electrolyser wired systems. More generally, this study indicates that both perovskite-based photovoltaic and photoelectrocatalytic systems have potential for large scale applications, as long as low-cost designs and the series resistance of the substrates are taken into account.

Acknowledgements

V.A. is grateful for the financial support from the Cambridge Trusts and the Winton Programme for the Physics of Sustainability. R.L.Z.H. acknowledges support from Magdalene College, Cambridge. This work was supported by the People Programme (Marie Curie Actions) of the European Union's Seventh Framework Programme FP7-PEOPLE-2013-IEF under REA Grant Agreement No. (623061; M.C.-Q.) and the Christian Doppler Research Association (Austrian Federal Ministry of Science, Research and Economy and the National Foundation for Research, Technology and Development) and the OMV Group (E.R.). S.A. and M.D.V. acknowledge financial support from an ERC Starting Grant (337739 HIENA). We gratefully acknowledge Prof. Dominic S. Wright (University of Cambridge) for providing us the TiCo single source precursor. We also thank Andreas Wagner and Esther E. Moore (University of Cambridge) for useful feedback, David Palm (Stanford University) for valuable insights into the $BiVO_4$ deposition and T. Jesper Jacobsson (University of Cambridge) for initial help with the perovskite preparation and Matlab scripts for analysing the raw photovoltaic data.

Author contributions

V.A. and E.R. designed the project. V.A. and R.L.Z.H. optimized the perovskite cells. V.A., M.C.-Q. and S.A. developed the photoelectrodes. V.A. and M.B. assembled the 3D printed PEC cell. V.A. performed the water splitting experiments. All authors contributed to the creation of the manuscript. E.R. supervised the work.

References

[1] N. S. Lewis, D. G. Nocera, *Proc. Natl. Acad. Sci. U. S. A.* **2006**, *103*, 15729–15735.

[2] T. R. Cook, D. K. Dogutan, S. Y. Reece, Y. Surendranath, T. S. Teets, D. G. Nocera, *Chem. Rev.* **2010**, *110*, 6474–6502.

[3] V. Andrei, K. Bethke, K. Rademann, *Energy Environ. Sci.* **2016**, *9*, 1528–1532.

[4] Y. Zhang, M. Xie, V. Adamaki, H. Khanbareh, C. R. Bowen, *Chem. Soc. Rev.* **2017**, *46*, 7757–7786.

[5] H. L. Tuller, *Mater. Renewable Sustainable Energy* **2017**, *6*, 3.

[6] J.-M. Tarascon, M. Armand, *Nature* **2001**, *414*, 359–367.

[7] J. W. Choi, D. Aurbach, *Nat. Rev. Mater.* **2016**, *1*, 16013.

[8] S. Ahmad, C. George, D. J. Beesley, J. J. Baumberg, M. d. Volder, *Nano Letters* **2018**, *18*, 1856–1862.

[9] S. Piontek, C. Andronescu, A. Zaichenko, B. Konkena, K. junge Puring, B. Marler, H. Antoni, I. Sinev, M. Muhler, D. Mollenhauer, B. Roldan Cuenya, W. Schuhmann, U.-P. Apfel, *ACS Catal.* **2018**, *8*, 987–996.

[10] J. Jia, L. C. Seitz, J. D. Benck, Y. Huo, Y. Chen, J. W. D. Ng, T. Bilir, J. S. Harris, T. F. Jaramillo, *Nat. Commun.* **2016**, *7*, 13237.

[11] M. Crespo-Quesada, E. Reisner, *Energy Environ. Sci.* **2017**, *10*, 1116–1127.

[12] C. Xiang, A. Z. Weber, S. Ardo, A. Berger, Y. Chen, R. Coridan, K. T. Fountaine, S. Haussener, S. Hu, R. Liu, N. S. Lewis, M. A. Modestino, M. M. Shaner, M. R. Singh, J. C. Stevens, K. Sun, K. Walczak, *Angew. Chem. Int. Ed.* **2016**, *55*, 12974–12988.

[13] T. J. Jacobsson, V. Fjallstrom, M. Edoff, T. Edvinsson, *Energy Environ. Sci.* **2014**, *7*, 2056–2070.

[14] W. Shockley, H. J. Queisser, *J. Appl. Phys.* **1961**, *32*, 510–519.

[15] M. S. Prévot, K. Sivula, *J. Phys. Chem. C* **2013**, *117*, 17879–17893.

[16] M. A. Green, Y. Hishikawa, E. D. Dunlop, D. H. Levi, J. Hohl-Ebinger, A. W. Ho-Baillie, *Prog. Photovolt. Res. Appl.* **2018**, *26*, 3–12.

[17] S. Hu, C. Xiang, S. Haussener, A. D. Berger, N. S. Lewis, *Energy Environ. Sci.* **2013**, *6*, 2984–2993.

[18] S. Haussener, S. Hu, C. Xiang, A. Z. Weber, N. S. Lewis, *Energy Environ. Sci.* **2013**, *6*, 3605–3618.

[19] J. Ronge, T. Bosserez, D. Martel, C. Nervi, L. Boarino, F. Taulelle, G. Decher, S. Bordiga, J. A. Martens, *Chem. Soc. Rev.* **2014**, *43*, 7963–7981.

[20] D. G. Nocera, *Acc. Chem. Res.* **2012**, *45*, 767–776.

[21] F. F. Abdi, L. Han, A. H. M. Smets, M. Zeman, B. Dam, R. van de Krol, *Nat. Commun.* **2013**, *4*, 2195.

[22] L. Han, F. F. Abdi, R. van de Krol, R. Liu, Z. Huang, H.-J. Lewerenz, B. Dam, M. Zeman, A. H. M. Smets, *ChemSusChem* **2014**, *7*, 2832–2838.

[23] M. R. Shaner, K. T. Fountaine, S. Ardo, R. H. Coridan, H. A. Atwater, N. S. Lewis, *Energy Environ. Sci.* **2014**, *7*, 779–790.

[24] M. V. Sheridan, D. J. Hill, B. D. Sherman, D. Wang, S. L. Marquard, K.-R. Wee, J. F. Cahoon, T. J. Meyer, *Nano Lett.* **2017**, *17*, 2440–2446.

[25] J. H. Park, A. J. Bard, *Electrochem. Solid-State Lett.* **2006**, *9*, E5–E8.

[26] R. Brimblecombe, A. Koo, G. C. Dismukes, G. F. Swiegers, L. Spiccia, *ChemSusChem* **2010**, *3*, 1146–1150.

[27] J. K. Kim, K. Shin, S. M. Cho, T.-W. Lee, J. H. Park, *Energy Environ. Sci.* **2011**, *4*, 1465–1470.

[28] J. Brillet, J.-H. Yum, M. Cornuz, T. Hisatomi, R. Solarska, J. Augustynski, M. Grätzel, K. Sivula, *Nat. Photonics* **2012**, *6*, 824.

[29] K. Shin, J.-B. Yoo, J. H. Park, *J. Power Sources* **2013**, *225*, 263–268.

[30] V. González-Pedro, I. Zarazua, E. M. Barea, F. Fabregat-Santiago, E. de la Rosa, I. Mora-Seró, S. Giménez, *J. Phys. Chem. C* **2014**, *118*, 891–895.

[31] K. Shin, J. H. Park, *ACS Appl. Mater. Interfaces* **2015**, *7*, 18429–18434.

[32] X. Shi, K. Zhang, K. Shin, M. Ma, J. Kwon, I. T. Choi, J. K. Kim, H. K. Kim, D. H. Wang, J. H. Park, *Nano Energy* **2015**, *13*, 182–191.

[33] B. D. Sherman, J. J. Bergkamp, C. L. Brown, A. L. Moore, D. Gust, T. A. Moore, *Energy Environ. Sci.* **2016**, *9*, 1812–1817.

[34] B. D. Sherman, M. V. Sheridan, K.-R. Wee, S. L. Marquard, D. Wang, L. Alibabaei, D. L. Ashford, T. J. Meyer, *J. Am. Chem. Soc.* **2016**, *138*, 16745–16753.

[35] X. Shi, H. Jeong, S. J. Oh, M. Ma, K. Zhang, J. Kwon, I. T. Choi, I. Y. Choi, H. K. Kim, J. K. Kim, J. H. Park, *Nat. Commun.* **2016**, *7*, 11943.

[36] S. Licht, B. Wang, S. Mukerji, T. Soga, M. Umeno, H. Tributsch, *J. Phys. Chem. B* **2000**, *104*, 8920–8924.

[37] A. Stavrides, A. Kunrath, J. Hu, R. Treglio, A. Feldman, B. Marsen, B. Cole, E. Miller, A. Madan, *Proc.SPIE* **2006**, *6340*, 63400K.

[38] J. Ziegler, B. Kaiser, W. Jaegermann, F. Urbain, J.-P. Becker, V. Smirnov, F. Finger, *ChemPhysChem* **2014**, *15*, 4026–4031.

[39] F. Urbain, V. Smirnov, J.-P. Becker, U. Rau, J. Ziegler, B. Kaiser, W. Jaegermann, F. Finger, *Sol. Energy Mater. Sol. Cells* **2015**, *140*, 275–280.

[40] M. M. May, H.-J. Lewerenz, D. Lackner, F. Dimroth, T. Hannappel, *Nat. Commun.* **2015**, *6*, 8286.

[41] W. B. Ingler, S. U. Khan, *Electrochem. Solid-State Lett.* **2006**, *9*, G144–G146.

[42] C.-Y. Lin, Y.-H. Lai, D. Mersch, E. Reisner, *Chem. Sci.* **2012**, *3*, 3482–3487.

[43] L. Tong, A. Iwase, A. Nattestad, U. Bach, M. Weidelener, G. Gotz, A. Mishra, P. Bauerle, R. Amal, G. G. Wallace, A. J. Mozer, *Energy Environ. Sci.* **2012**, *5*, 9472–9475.

[44] K. Fan, F. Li, L. Wang, Q. Daniel, E. Gabrielsson, L. Sun, *Phys. Chem. Chem. Phys.* **2014**, *16*, 25234–25240.

[45] P. Bornoz, F. F. Abdi, S. D. Tilley, B. Dam, R. van de Krol, M. Grätzel, K. Sivula, *J. Phys. Chem. C* **2014**, *118*, 16959–16966.

[46] F. Li, K. Fan, B. Xu, E. Gabrielsson, Q. Daniel, L. Li, L. Sun, *J. Am. Chem. Soc.* **2015**, *137*, 9153–9159.

[47] Y.-H. Lai, D. W. Palm, E. Reisner, *Adv. Energy Mater.* **2015**, *5*, 1501668.

[48] P. Xu, J. Feng, T. Fang, X. Zhao, Z. Li, Z. Zou, *RSC Adv.* **2016**, *6*, 9905–9910.

[49] N. Kornienko, N. A. Gibson, H. Zhang, S. W. Eaton, Y. Yu, S. Aloni, S. R. Leone, P. Yang, *ACS Nano* **2016**, *10*, 5525–5535.

[50] A. Kargar, J. Khamwannah, C.-H. Liu, N. Park, D. Wang, S. A. Dayeh, S. Jin, *Nano Energy* **2016**, *19*, 289–296.

[51] A. Kojima, K. Teshima, Y. Shirai, T. Miyasaka, *J. Am. Chem. Soc.* **2009**, *131*, 6050–6051.

[52] National Renewable Energy Laboratory, *Best Research-Cell Efficiencies*, **2017**, `https://www.nrel.gov/pv/assets/images/efficiency-chart.png`.

[53] J. Luo, J.-H. Im, M. T. Mayer, M. Schreier, M. K. Nazeeruddin, N.-G. Park, S. D. Tilley, H. J. Fan, M. Grätzel, *Science* **2014**, *345*, 1593–1596.

[54] J. Luo, Z. Li, S. Nishiwaki, M. Schreier, M. T. Mayer, P. Cendula, Y. H. Lee, K. Fu, A. Cao, M. K. Nazeeruddin, Y. E. Romanyuk, S. Buecheler, S. D. Tilley, L. H. Wong, A. N. Tiwari, M. Grätzel, *Adv. Energy Mater.* **2015**, *5*, 1501520.

[55] J. Luo, D. A. Vermaas, D. Bi, A. Hagfeldt, W. A. Smith, M. Grätzel, *Adv. Energy Mater.* **2016**, *6*, 1600100.

[56] A. R. Bin, M. Yusoff, J. Jang, *Chem. Commun.* **2016**, *52*, 5824–5827.

[57] T. Sharifi, C. Larsen, J. Wang, W. L. Kwong, E. Gracia-Espino, G. Mercier, J. Messinger, T. Wågberg, L. Edman, *Adv. Energy Mater.* **2016**, *6*, 1600738.

[58] M. Schreier, L. Curvat, F. Giordano, L. Steier, A. Abate, S. M. Zakeeruddin, J. Luo, M. T. Mayer, M. Grätzel, *Nat. Commun.* **2015**, *6*, 7326.

[59] W. Ma, J. Han, W. Yu, D. Yang, H. Wang, X. Zong, C. Li, *ACS Catal.* **2016**, *6*, 6198–6206.

[60] K. S. Joya, Y. F. Joya, K. Ocakoglu, R. van de Krol, *Angew. Chem. Int. Ed.* **2013**, *52*, 10426–10437.

[61] J. H. Kim, Y. Jo, J. H. Kim, J. W. Jang, H. J. Kang, Y. H. Lee, D. S. Kim, Y. Jun, J. S. Lee, *ACS Nano* **2015**, *9*, 11820–11829.

[62] Gurudayal, D. Sabba, M. H. Kumar, L. H. Wong, J. Barber, M. Grätzel, N. Mathews, *Nano Lett.* **2015**, *15*, 3833–3839.

[63] Y.-S. Chen, J. S. Manser, P. V. Kamat, *J. Am. Chem. Soc.* **2015**, *137*, 974–981.

[64] X. Zhang, B. Zhang, K. Cao, J. Brillet, J. Chen, M. Wang, Y. Shen, *J. Mater. Chem. A* **2015**, *3*, 21630–21636.

[65] Y. Qiu, W. Liu, W. Chen, G. Zhou, P.-C. Hsu, R. Zhang, Z. Liang, S. Fan, Y. Zhang, Y. Cui, *Sci. Adv.* **2016**, *2*, e1501764.

[66] J. H. Baek, B. J. Kim, G. S. Han, S. W. Hwang, D. R. Kim, I. S. Cho, H. S. Jung, *ACS Appl. Mater. Interfaces* **2017**, *9*, 1479–1487.

[67] A. Kafizas, L. Francàs, C. Sotelo-Vazquez, M. Ling, Y. Li, E. Glover, L. McCafferty, C. Blackman, J. Darr, I. Parkin, *J. Phys. Chem. C* **2017**, *121*, 5983–5993.

[68] B. Sun, T. Shi, Z. Liu, Z. Tang, J. Zhou, G. Liao, *RSC Adv.* **2016**, *6*, 110120–110126.

[69] C. G. Morales-Guio, M. T. Mayer, A. Yella, S. D. Tilley, M. Grätzel, X. Hu, *J. Am. Chem. Soc.* **2015**, *137*, 9927–9936.

[70] Gurudayal, R. A. John, P. P. Boix, C. Yi, C. Shi, M. C. Scott, S. A. Veldhuis, A. M. Minor, S. M. Zakeeruddin, L. H. Wong, M. Grätzel, N. Mathews, *ChemSusChem* **2017**, *10*, 2449–2456.

[71] Y. J. Jang, I. Jeong, J. Lee, J. Lee, M. J. Ko, J. S. Lee, *ACS Nano* **2016**, *10*, 6980–6987.

[72] P. Da, M. Cha, L. Sun, Y. Wu, Z.-S. Wang, G. Zheng, *Nano Lett.* **2015**, *15*, 3452–3457.

[73] M. T. Hoang, N. D. Pham, J. H. Han, J. M. Gardner, I. Oh, *ACS Appl. Mater. Interfaces* **2016**, *8*, 11904–11909.

[74] C. Wang, S. Yang, X. Chen, T. Wen, H. G. Yang, *J. Mater. Chem. A* **2017**, *5*, 910–913.

[75] M. Crespo-Quesada, L. M. Pazos-Outón, J. Warnan, M. F. Kuehnel, R. H. Friend, E. Reisner, *Nat. Commun.* **2016**, *7*, 12555.

[76] J. Burschka, N. Pellet, S.-J. Moon, R. Humphry-Baker, P. Gao, M. K. Nazeeruddin, M. Grätzel, *Nature* **2013**, *499*, 316–319.

[77] N. J. Jeon, J. H. Noh, W. S. Yang, Y. C. Kim, S. Ryu, J. Seo, S. I. Seok, *Nature* **2015**, *517*, 476–480.

[78] T. J. Jacobsson, J.-P. Correa-Baena, M. Pazoki, M. Saliba, K. Schenk, M. Grätzel, A. Hagfeldt, *Energy Environ. Sci.* **2016**, *9*, 1706–1724.

[79] M. Saliba, T. Matsui, J.-Y. Seo, K. Domanski, J.-P. Correa-Baena, M. K. Nazeeruddin, S. M. Zakeeruddin, W. Tress, A. Abate, A. Hagfeldt, M. Grätzel, *Energy Environ. Sci.* **2016**, *9*, 1989–1997.

[80] M. Saliba, T. Matsui, K. Domanski, J.-Y. Seo, A. Ummadisingu, S. M. Zakeeruddin, J.-P. Correa-Baena, W. R. Tress, A. Abate, A. Hagfeldt, M. Grätzel, *Science* **2016**, *354*, 206–209.

[81] Z. Tang, T. Bessho, F. Awai, T. Kinoshita, M. M. Maitani, R. Jono, T. N. Murakami, H. Wang, T. Kubo, S. Uchida, H. Segawa, *Sci. Rep.* **2017**, *7*, 12183.

[82] T. Bu, X. Liu, Y. Zhou, J. Yi, X. Huang, L. Luo, J. Xiao, Z. Ku, Y. Peng, F. Huang, Y.-B. Cheng, J. Zhong, *Energy Environ. Sci.* **2017**, *10*, 2509–2515.

[83] S.-H. Turren-Cruz, M. Saliba, M. T. Mayer, H. Juarez-Santiesteban, X. Mathew, L. Nienhaus, W. Tress, M. P. Erodici, M.-J. Sher, M. G. Bawendi, M. Grätzel, A. Abate, A. Hagfeldt, J.-P. Correa-Baena, *Energy Environ. Sci.* **2018**, *11*, 78–86.

[84] D.-Y. Son, S.-G. Kim, J.-Y. Seo, S.-H. Lee, H. Shin, D. Lee, N.-G. Park, *J. Am. Chem. Soc.* **2018**, *140*, 1358–1364.

[85] T. J. Jacobsson, S. Svanström, V. Andrei, J. P. H. Rivett, N. Kornienko, B. Philippe, U. B. Cappel, H. Rensmo, F. Deschler, G. Boschloo, *J. Phys. Chem. C* **2018**. DOI: 10.1021/acs.jpcc.7b12464.

[86] Z. Yang, S. Zhang, L. Li, W. Chen, *J. Materiomics* **2017**, *3*, 231–244.

[87] G. Kakavelakis, I. Paradisanos, B. Paci, A. Generosi, M. Papachatzakis, T. Maksudov, L. Najafi, A. E. Del Rio Castillo, G. Kioseoglou, E. Stratakis, F. Bonaccorso, E. Kymakis, *Adv. Energy Mater.* **2018**, 1702287.

[88] Y. Hu, S. Si, A. Mei, Y. Rong, H. Liu, X. Li, H. Han, *Sol. RRL* **2017**, *1*, 1600019.

[89] A. Abate, J.-P. Correa-Baena, M. Saliba, M. S. Su'ait, F. Bella, *Chem. - Eur. J.* **2018**, *24*, 3083–3100.

[90] R. L. Z. Hoye, L. C. Lee, R. C. Kurchin, T. N. Huq, K. H. L. Zhang, M. Sponseller, L. Nienhaus, R. E. Brandt, J. Jean, J. A. Polizzotti, A. Kursumović, M. G. Bawendi, V. Bulović, V. Stevanović, T. Buonassisi, J. L. MacManus-Driscoll, *Adv. Mater.* **2017**, *29*, 1702176.

[91] Y. Kuang, Q. Jia, H. Nishiyama, T. Yamada, A. Kudo, K. Domen, *Adv. Energy Mater.* **2016**, *6*, 1501645.

[92] K. P. Sokol, D. Mersch, V. Hartmann, J. Z. Zhang, M. M. Nowaczyk, M. Rogner, A. Ruff, W. Schuhmann, N. Plumere, E. Reisner, *Energy Environ. Sci.* **2016**, *9*, 3698–3709.

[93] R. Sander, *Atmos. Chem. Phys.* **2015**, *15*, 4399–4981.

[94] A. Ambrosi, J. G. S. Moo, M. Pumera, *Adv. Funct. Mater.* **2016**, *26*, 698–703.

[95] A. Ambrosi, M. Pumera, *Adv. Funct. Mater.* **2017**, 1700655.

[96] L. F. Arenas, C. Ponce de León, F. C. Walsh, *Electrochem. Commun.* **2017**, *77*, 133–137.

[97] M. D. Symes, P. J. Kitson, J. Yan, C. J. Richmond, G. J. T. Cooper, R. W. Bowman, T. Vilbrandt, L. Cronin, *Nat. Chem.* **2012**, *4*, 349.

[98] B. D. Gould, J. A. Rodgers, M. Schuette, K. Bethune, S. Louis, R. Rocheleau, K. Swider-Lyons, *ECS J. Solid State Sci. Technol.* **2015**, *4*, P3063–P3068.

[99] R. Porta, M. Benaglia, A. Puglisi, *Org. Process Res. Dev.* **2016**, *20*, 2–25.

[100] A. A. Folgueiras-Amador, K. Philipps, S. Guilbaud, J. Poelakker, T. Wirth, *Angew. Chem. Int. Ed.* **2017**, *56*, 15446–15450.

[101] J. T. Davis, D. V. Esposito, *J. Phys. D Appl. Phys.* **2017**, *50*, 084002.

[102] Y. Zhou, C. Fuentes-Hernandez, J. Shim, J. Meyer, A. J. Giordano, H. Li, P. Winget, T. Papadopoulos, H. Cheun, J. Kim, M. Fenoll, A. Dindar, W. Haske, E. Najafabadi, T. M. Khan, H. Sojoudi, S. Barlow, S. Graham, J.-L. Brédas, S. R. Marder, A. Kahn, B. Kippelen, *Science* **2012**, *336*, 327–332.

[103] A. Guerrero, J. You, C. Aranda, Y. S. Kang, G. Garcia-Belmonte, H. Zhou, J. Bisquert, Y. Yang, *ACS Nano* **2016**, *10*, 218–224.

[104] J.-Y. Jeng, K.-C. Chen, T.-Y. Chiang, P.-Y. Lin, T.-D. Tsai, Y.-C. Chang, T.-F. Guo, P. Chen, T.-C. Wen, Y.-J. Hsu, *Adv. Mater.* **2014**, *26*, 4107–4113.

[105] W. C. Lai, K. W. Lin, T. F. Guo, J. Lee, *IEEE Trans. Electron Devices* **2015**, *62*, 1590–1595.

[106] J. H. Kim, P.-W. Liang, S. T. Williams, N. Cho, C.-C. Chueh, M. S. Glaz, D. S. Ginger, A. K.-Y. Jen, *Adv. Mater.* **2015**, *27*, 695–701.

[107] J. You, L. Meng, T.-B. Song, T.-F. Guo, Y. Yang, W.-H. Chang, Z. Hong, H. Chen, H. Zhou, Q. Chen, Y. Liu, N. d. Marco, *Nat. Nanotechnol.* **2016**, *11*, 75–81.

[108] M.-H. Liu, Z.-J. Zhou, P.-P. Zhang, Q.-W. Tian, W.-H. Zhou, D.-X. Kou, S.-X. Wu, *Opt. Express* **2016**, *24*, A1349–A1359.

[109] E. Lorenzo, *Solar Electricity: Engineering of Photovoltaic Systems*, PROGENSA, **1994**.

[110] A. Luque, S. Hegedus, *Handbook of photovoltaic science and engineering*, Wiley, Chichester, West Sussex, U.K, 2nd ed., **2011**.

[111] T. Liu, K. Chen, Q. Hu, R. Zhu, Q. Gong, *Adv. Energy Mater.* **2016**, *6*, 1600457.

[112] J. Seo, J. H. Noh, S. I. Seok, *Acc. Chem. Res.* **2016**, *49*, 562–572.

[113] V. Andrei, K. Bethke, F. Madzharova, S. Beeg, A. Knop-Gericke, J. Kneipp, K. Rademann, *Adv. Electron. Mater.* **2017**, 1600473.

[114] J. A. Seabold, K.-S. Choi, *J. Am. Chem. Soc.* **2012**, *134*, 2186–2192.

[115] Y. Park, K. J. McDonald, K.-S. Choi, *Chem. Soc. Rev.* **2013**, *42*, 2321–2337.

[116] X. Shi, I. Y. Choi, K. Zhang, J. Kwon, D. Y. Kim, J. K. Lee, S. H. Oh, J. K. Kim, J. H. Park, *Nat. Commun.* **2014**, *5*, 4775.

[117] K. R. Tolod, S. Hernández, N. Russo, *Catalysts* **2017**, *7*, 13.

[118] T. W. Kim, K.-S. Choi, *Science* **2014**, *343*, 990–994.

[119] L. Zhang, E. Reisner, J. J. Baumberg, *Energy Environ. Sci.* **2014**, *7*, 1402–1408.

[120] L. Zhang, C.-Y. Lin, V. K. Valev, E. Reisner, U. Steiner, J. J. Baumberg, *Small* **2014**, *10*, 3970–3978.

[121] A. Shinde, D. Guevarra, G. Liu, I. D. Sharp, F. M. Toma, J. M. Gregoire, J. A. Haber, *ACS Appl. Mater. Interfaces* **2016**, *8*, 23696–23705.

[122] F. F. Abdi, N. Firet, R. van de Krol, *ChemCatChem* **2013**, *5*, 490–496.

[123] S. Y. Reece, J. A. Hamel, K. Sung, T. D. Jarvi, A. J. Esswein, Pijpers, Joep J. H., D. G. Nocera, *Science* **2011**, *334*, 645–648.

[124] C. Hu, X. Chen, Q. Dai, M. Wang, L. Qu, L. Dai, *Nano Energy* **2017**, *41*, 367–376.

[125] S. K. Kuk, R. K. Singh, D. H. Nam, R. Singh, J.-K. Lee, C. B. Park, *Angew. Chem. Int. Ed.* **2017**, *56*, 3827–3832.

[126] D. H. Nam, G. M. Ryu, S. K. Kuk, D. S. Choi, E. J. Son, C. B. Park, *Appl. Catal. B Environ.* **2016**, *198*, 311–317.

[127] I. Holmes-Gentle, F. Hoffmann, C. A. Mesa, K. Hellgardt, *Sustainable Energy Fuels* **2017**, *1*, 1184–1198.

[128] C. Carver, Z. Ulissi, C. K. Ong, S. Dennison, G. H. Kelsall, K. Hellgardt, *Int. J. Hydrogen Energy* **2012**, *37*, 2911–2923.

[129] A. Hankin, F. E. Bedoya-Lora, C. K. Ong, J. C. Alexander, F. Petter, G. H. Kelsall, *Energy Environ. Sci.* **2017**, *10*, 346–360.

[130] W. J. Lee, P. S. Shinde, G. H. Go, E. Ramasamy, *Int. J. Hydrogen Energy* **2011**, *36*, 5262–5270.

[131] D. Zhao, M. Sexton, H.-Y. Park, G. Baure, J. C. Nino, F. So, *Adv. Energy Mater.* **2015**, *5*, 1401855.

[132] J. T.-W. Wang, Z. Wang, S. Pathak, W. Zhang, D. W. deQuilettes, F. Wisnivesky-Rocca-Rivarola, J. Huang, P. K. Nayak, J. B. Patel, H. A. Mohd Yusof, Y. Vaynzof, R. Zhu, I. Ramirez, J. Zhang, C. Ducati, C. Grovenor, M. B. Johnston, D. S. Ginger, R. J. Nicholas, H. J. Snaith, *Energy Environ. Sci.* **2016**, *9*, 2892–2901.

[133] V. Andrei, K. Bethke, F. Madzharova, A. C. Bronneberg, J. Kneipp, K. Rademann, *ACS Appl. Mater. Interfaces* **2017**, *9*, 33308–33316.

[134] J. Zhao, Y. Guo, L. Cai, H. Li, K. X. Wang, I. S. Cho, C. H. Lee, S. Fan, X. Zheng, *ACS Energy Lett.* **2016**, *1*, 68–75.

[135] N. Iqbal, I. Khan, Z. H. A. Yamani, A. Qurashi, *Sol. Energy* **2017**, *144*, 604–611.

[136] C. Roldan-Carmona, O. Malinkiewicz, A. Soriano, G. Minguez Espallargas, A. Garcia, P. Reinecke, T. Kroyer, M. I. Dar, M. K. Nazeeruddin, H. J. Bolink, *Energy Environ. Sci.* **2014**, *7*, 994–997.

[137] M. Kaltenbrunner, G. Adam, E. D. Glowacki, M. Drack, R. Schwodiauer, L. Leonat, D. H. Apaydin, H. Groiss, M. C. Scharber, M. S. White, N. S. Sariciftci, S. Bauer, *Nat. Mater.* **2015**, *14*, 1032–1039.

[138] V. Andrei, K. Bethke, K. Rademann, *Phys. Chem. Chem. Phys.* **2016**, *18*, 10700–10707.